Vulnerable Atherosclerotic Plaque Elasticity Reconstruction Based on a Segmentation-Driven Optimization Procedure Using Strain Measurements: Theoretical Framework

Simon Le Floc'h, Jacques Ohayon*, Philippe Tracqui, Gérard Finet, Ahmed M. Gharib, Roch L. Maurice, Guy Cloutier, and Roderic I. Pettigrew

Abstract—It is now recognized that prediction of the vulnerable coronary plaque rupture requires not only an accurate quantification of fibrous cap thickness and necrotic core morphology but also a precise knowledge of the mechanical properties of plaque components. Indeed, such knowledge would allow a precise evaluation of the peak cap-stress amplitude, which is known to be a good biomechanical predictor of plaque rupture. Several studies have been performed to reconstruct a Young's modulus map from strain elastograms. It seems that the main issue for improving such methods does not rely on the optimization algorithm itself, but rather on preconditioning requiring the best estimation of the plaque components' contours. The present theoretical study was therefore designed to develop: 1) a preconditioning model to extract the plaque morphology in order to initiate the optimization process, and 2) an approach combining a dynamic segmentation method with an optimization procedure to highlight the modulogram of the atherosclerotic plaque. This methodology, based on the continuum mechanics theory prescribing the strain field, was successfully applied to seven intravascular ultrasound coronary lesion morphologies. The reconstructed cap thickness, necrotic core area, calcium area, and the Young's moduli of the calcium, necrotic core, and fibrosis were obtained with mean relative errors of 12%, 4% and 1%, 43%, 32%, and 2%, respectively.

Index Terms—Coronary arteries, elastography, inverse problem, linear elasticity, modulography, vulnerable plaques.

S. Le Floc'h and P. Tracqui are with the Laboratory TIMC, DynaCell, CNRS UMR 5525, Institut de l'Ingénierie et de l'Information de Santé (In3S), 38 706 Grenoble, France.

*J. Ohayonis with the Laboratory TIMC, DynaCell, CNRS UMR 5525, Institut de l'Ingénierie et de l'Information de Santé (In3S), Grenoble, France, and also with the National Institute of Diabetes and Digestive and Kidney Diseases, National Institutes of Health, Bethesda, MD 20892 USA (e-mail: ohayonj2@mail.nih.gov).

G. Finet is with the Department of Hemodynamics and Interventional Cardiology, Hospices Civils de Lyon and Claude Bernard University Lyon 1; INSERM Unit 886,69394 Lyon, France.

G. Cloutier is with the Laboratory of Biorheology and Medical Ultrasonics, Research Center, University of Montreal Hospital (CRCHUM), Montréal, H2L 2W5 QC, Canada (e-mail: guy.cloutier@umontreal.ca).

R. L. Maurice is with the Department of Radiology, Radio-Oncology and Nuclear Medicine, and Institute of Biomedical Engineering, University of Montreal, H2L 2W5 QC, Canada.

A. M. Gharib and R. I. Pettigrew are with the National Institute of Diabetes and Digestive and Kidney Diseases, National Institutes of Health, Bethesda, MD 20892 USA (e-mail: rpettig@mail.nih.gov).

Color versions of one or more of the figures in this paper are available online at http://ieeexplore.ieee.org.

Digital Object Identifier 10.1109/TMI.2009.2012852

I. INTRODUCTION

ATHEROSCLEROTIC plaque rupture is a recognized major cause of acute coronary syndrome [1], [2]. Histological studies [1], [3], [4] have shown that a vulnerable coronary plaque is typically defined by a large extracellular necrotic core and a thin fibrous cap infiltrated by macrophages. Rupture of the cap induces the formation of a thrombus which may obstruct the coronary artery, causing an acute syndrome and the patient death.

Several reports revealed that such vulnerable plaques can be detected clinically by various techniques, including intravascular ultrasound (IVUS) [5], [6], optical coherence tomography (OCT) [7], [8], computed tomography [9], and magnetic resonance imaging (MRI) [10]. However, usual prediction of rupture based on imaging of the plaque morphology and composition [11], [12] still provides rather imprecise and insufficient predictors of risk. The challenge for imaging methods is that prediction of the coronary plaque rupture requires not only an accurate quantification of fibrous cap thickness [13] and necrotic core morphology [14], but also a precise knowledge of the mechanical properties of the arterial wall and plaque components at any given stage of the plaque growth and remodeling [11], [15]–[18]. Indeed, such knowledge can allow a precise evaluation of the thin-cap fibro-atheroma peak stress amplitude, which appears to be a good biomechanical predictor of plaque rupture [11], [15].

Unfortunately, analysis of plaque mechanical properties is difficult due to its heterogeneity. More precisely, establishing a modulogram of a plaque, i.e., an elasticity map, constitutes a prerequisite for a reliable computation of intraplaque stresses. Computation of such modulograms is a challenge that has been tackled by a rather large diversity of approaches. Based on the estimation of the strain field inside the atheroma plaque obtained from various ultrasound-based techniques [19]–[22] and

OCT [23]–[25], several studies have been performed to estimate vascular elasticity maps [20], [22], [26]–[39]. Either direct approaches [20], [34], [37] or iterative procedures [22], [26], [28]–[32], [35], [36], [38], [39] were proposed. The iterative approaches used a central core optimization algorithm to minimize the error between computed and measured strains or displacement fields. In this context, improvement of plaque elasticity reconstruction depends on the performance of the optimization procedure. Thus, several groups [29], [35], [38], [40] developed robust optimization algorithms for extracting elastic moduli of plaque components, assuming a known plaque morphology. However, it seems that the main issue for improving such methods does not mostly rely on the improvement of the optimization algorithm itself, but rather on the preconditioning of the algorithm based on the best estimation of the plaque components' contours, which is the main goal of the current study.

Still few studies have been conducted in this direction [28], [30]. Recently, Baldewsing *et al.* [41] developed and used successfully an elegant parametric finite element model (PFEM) to assess the morphology of a plaque composed of a unique necrotic core. Interestingly, this approach has been extended by the same group to the case of multiple necrotic cores: each core was considered separately and the solution was obtained by considering the superposition of noncorrelated inverse problems [28]. Despite its robustness, this PFEM has some limitations. Indeed, this method would not be efficient enough to extract the real morphology plaque exhibiting several neighboring necrotic cores and/or calcium inclusions, thus preventing a good diagnosis of plaque vulnerability.

The present theoretical study was therefore designed to determine the modulogram of complex atherosclerotic plaques by developing an original preconditioning step for the optimization process, and a new approach combining a dynamic watershed segmentation method with the optimization procedure to extract the morphology and Young's modulus of each plaque component. This combined approach, based on the continuum mechanics theory prescribing the strain field, was successfully applied to seven coronary lesions of patients imaged *in vivo* with IVUS. The robustness and performance of the method was investigated with regard to various factors which may affect prediction of plaque vulnerability.

II. MATERIALS AND METHODS

A series of patients underwent coronary IVUS to extract plaque morphologies that were used to simulate strain elastograms from which the performance of both Young's modulus and plaque geometry reconstructions method were tested. Moreover, two idealized cross-sectional plaque morphologies were designed to investigate the performance of the proposed algorithm when approximating the cap thickness value.

A. IVUS Study and Plaque Geometries

1) Patient Population: Arteries were explored in patients referred for percutaneous coronary intervention at the Lyon Cardiology Hospital (Hôpital Cardiologique et Pneumologique de
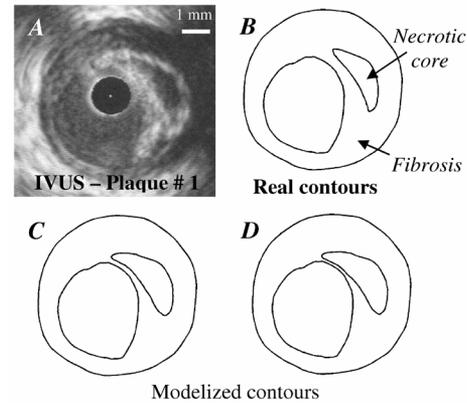

Fig. 1. (A) Typical *in-vivo* intravascular ultrasound image and (B) real contours of one fibrous-cap fibro-atheromatous plaque (Plaque #1, cap thickness $= 369 \, \mu$m). (C) and (D) Two idealized models in which the fibrous cap thickness decreases from $174 \, \mu$m to $103 \, \mu$m were manually traced by increasing the initial necrotic core size of Plaque #1.

Lyon, France) after a first acute coronary syndrome with troponin I elevation. Investigations were approved by the institutional board of the Hospital Cardiology Department and patients were studied only after giving informed consent.

2) Intravascular Ultrasound Imaging: A dataset of nonruptured vulnerable and stable plaques was obtained from systematic IVUS scans of the three principal coronary arteries following the protocol described by Rioufol *et al.* [6]. All patients were examined by IVUS after intracoronary administration of $200 \, \mu$g of nitroglycerine to avoid vasospasms. For each selected vulnerable lesion, the acquired cross-sectional IVUS image corresponded to the site exhibiting the thinner fibroatheroma cap. IVUS scans were performed with the iLab platform (Boston Scientific, Watertown, MA) equipped with 40 MHz catheters (Atlantis SR Pro 3.6F, Boston Scientific).

3) IVUS Image Analysis: IVUS coronary lesion images were saved onto a computer for postprocessing (SAMBA PDB 5.01 software, Grenoble, France). Plaque components were characterized by their IVUS aspect: 1) highly hypoechogenic components (or anechogenic zones), suggestive of quasi-cellular tissues (lipid or cellular deposition); 2) homogeneous reflective components, suggestive of organized or disorganized fibrosis; or 3) hyperechogenic components (or bright zones), suggestive of calcium [42]. A manual segmentation procedure using an image processing software (ImageJ, NIH, Bethesda, MD) was performed to extract the contours of each plaque component.

4) IVUS Measurements and Definitions: Each cross-sectional IVUS lesion image was quantified for plaque area ($\mathrm{Pla_{area}}$, mm^2), lumen area ($\mathrm{Lu_{area}}$, mm^2), necrotic core area ($\mathrm{Core_{area}}$, mm^2), cap thickness ($\mathrm{Cap_{thick}}$, mm), calcium area ($\mathrm{Cal_{area}}$, mm^2), and degree of stenosis ($\mathrm{Stenos_{deg}}$, %) as $100 \times \mathrm{Pla_{area}}/(\mathrm{Pla_{area}} + \mathrm{Lu_{area}})$. Cap thickness was defined as the shortest distance between the lumen and the necrotic core.

5) Idealized Geometries: From one real nonruptured vulnerable plaque geometry acquired on a patient by IVUS, two idealized models mimicking the plaque evolution by increasing the initial $\mathrm{Core_{area}}$ and decreasing the $\mathrm{Cap_{thick}}$ values (Fig. 1) were designed.

B. Forward Problem: Spatial Strain Distribution From Structural Analysis

Static Finite Element (FE) computations were performed on all real and idealized plaque geometries. The spatial strain distributions were calculated using COMSOL Multiphysics software (Structural Mechanics Module, version 3.3, COMSOL, France). The plaque geometries were meshed with approximately 15 000 6-node triangular elements.

1) Boundary Conditions and Material Properties: The FE models were solved under the assumption of plane strain and a blood pressure differential of 1 kPa (or 7.5 mmHg) was applied which corresponds to a realistic pressure gradient occurring between two successive IVUS images recorded during the systolic phases (i.e., left ventricular isovolumic contraction and ejection phases). To avoid all kind of rigid body translations and rotations, we considered two opposite nodes where displacement conditions were prescribed: one node was completely fixed, and the other one was prevented from displacing in the tangential direction. Everywhere else on the external diameter of the artery, free boundary conditions were considered.

The fibrosis, calcium and soft necrotic core were modeled as isotropic quasi-incompressible solids (Poisson's ratio $\nu = 0.49$) with Young's moduli $E_{\text{fibrosis}} = 600$ kPa, $E_{\text{calcium}} = 5000$ kPa and $E_{\text{core}} = 10$ kPa, respectively [16]. Additional simulations were performed to investigate the influence of a potential surrounding tissue by considering an external layer of variable relative thickness (varying from 1.5 to 10) modeled also as a quasi-incompressible isotropic medium (Poisson's ratio $\nu = 0.49$) with Young's modulus ranging from 1 to 600 kPa. The relative thickness is defined as the ratio between the radius of the surrounding tissue and the mean radius of the artery. Except when explicitly mentioned, computations were performed without surrounding tissue.

2) Intraplaque Strain Distribution: The center of gravity of the lumen was used as the origin of the cylindrical coordinate system. The strain fields were interpolated on a regular polar mesh with a given radial step resolution of 36 μm and an angular step resolution corresponding to 256 radial directions, which is the resolution one can expect from endovascular elastography [21]. The default catheter position was located at the origin of the cylindrical system.

Sensitivity study with regard to catheter position—The *in vivo* situation shows that the catheter position is often off-centered. The fact that the catheter is not centered may affect the intraplaque strain distribution (called also strain artifact) and could influence the plaque characterization [43]. To investigate such effects, we simulated the radial strain fields for four different angular positions of the off-centered catheter and reconstructed the Young's modulus repartition from these perturbed strain fields. The catheter positions were calculated using an eccentricity of 1 mm (the eccentricity was defined as the distance between the center of the catheter and the center of gravity of the lumen in the cross section of interest).

Sensitivity study with regard to noise on input strain data—To further evaluate the performance of our method, a default white-noise was added to each FE simulated strain field used as input. The noise model was based on the work of Baldewsing *et al.* [43], who used a normal distribution of noise with zero mean and a standard deviation of $(a\,\varepsilon_{rr} + b)\,\beta$, with $a = 0.2\%$, $b = 0.04\%$ and where ε_{rr} is the local value of the radial strain. To investigate the influence of the white noise on the stability and convergence of our algorithm, the default noise field ($\beta = 1$) was significantly amplified by increasing β from 1 to 6. Knowing that this noise was spatially randomly distributed, we averaged the results obtained from the reconstruction procedure by performing 15 computations for each level of noise.

C. Inverse Problem: Elasticity Map

1) Contour Detection Algorithms Based on Continuum Mechanics Theory: Skovoroda's transform (SkT)—Skovoroda *et al.* [44] proposed a mathematical criterion to extract the inclusion contours, knowing the intraplaque strain field and using the equation of local stress continuity at the interface between inclusions and surrounding media with Young's moduli E^{int} and E^{ext}, respectively. The detection of each contour point was performed by estimating the ratio of internal $\varepsilon_{\text{ij}}^{\text{int}}$ over external $\varepsilon_{\text{ij}}^{\text{ext}}$ strain components along an arbitrary direction and in an infinitesimal region. Thus, the location of the maximum ratios highlighted the inclusion contours. The simplified mathematical expression of their criterion [44]—obtained when the material is assumed incompressible and when only the radial component of the strain tensor ε_{rr} is considered—is given by

$$\frac{E^{\text{ext}}}{E^{\text{int}}} = \frac{\varepsilon_{rr}^{\text{int}}}{\varepsilon_{rr}^{\text{ext}}}. \tag{1}$$

In this study, we used this criterion to evaluate the improvement provided by the extension of the Sumi's transform that is proposed below.

Modified Sumi's transform (MST)—Assuming that the mechanical properties vary continuously in space and by writing the local equilibrium equation for isotropic incompressible media solicited under plane stress condition, Sumi *et al.* [45] found a relationship between the vector gradient of the Young modulus and the strain tensor components. This criterion was used successfully to reconstruct the rigidity map in the case of a circular heterogeneity immerged in a continuum medium [45]. However, note that the plane stress condition is not relevant to model a blood vessel deformation. Therefore, we extended their approach to elastic media loaded under plane strain condition. Considering that the plaque is incompressible, we derived the expression of the Young's modulus gradient in the following way.

Assuming linear elasticity, the heterogeneous medium is described by the Hooke's law

$$[\sigma] = -p\,[I] + \frac{2}{3}E(\vec{x})\,[\varepsilon] \tag{2}$$

where $[\sigma]$ and $[\varepsilon]$ are the stress and strain tensors, $[I]$ is the identity matrix, E the Young's modulus which is an arbitrary function of the position vector $\vec{x}$ and p the Lagrangian multiplier resulting from the incompressibility of the material given by the following kinematics constraint [46]

$$\text{Trace}\,[\varepsilon] = 0. \tag{3}$$

Neglecting gravity and inertial forces, the stress tensor $[\sigma]$ satisfies the local equilibrium equation

$$\nabla.[\sigma] = \vec{0}. \tag{4}$$

Substituting (2) and (3) into (4) allowed to obtain the Young's modulus gradient through the relationship

$$\frac{\nabla E}{E} = \frac{3}{2}[\varepsilon]^{-1}\frac{\nabla p}{E} - [\varepsilon]^{-1}\nabla.[\varepsilon]. \tag{5}$$

Since the components of the Lagrange multiplier gradient cannot be measured experimentally, focusing on the second term of (5) right hand side becomes *a priori* a natural choice for highlighting Young's modulus discontinuity boundaries. Therefore we introduced the vector defined by

$$\vec{H} = -[\varepsilon]^{-1}\nabla.[\varepsilon]. \tag{6}$$

The successful reconstructions of the inclusions maps validate a posteriori the relevance and efficiency of this expression for driving the segmentation procedure. Using the equation of incompressibility (i.e., (3) or $\varepsilon_{\theta\theta} = -\varepsilon_{rr}$), the two components of $\vec{H}$ may be rewritten in the 2D polar coordinate system (r, θ), as follows:

$$H_r = -\frac{1}{\varepsilon_{rr}^2 + \varepsilon_{r\theta}^2}\left\{\varepsilon_{rr}\left(\frac{\partial\varepsilon_{rr}}{\partial r} + \frac{1}{r}\frac{\partial\varepsilon_{r\theta}}{\partial\theta} + \frac{2\varepsilon_{rr}}{r}\right)\right.$$
$$\left. + \varepsilon_{r\theta}\left(\frac{\partial\varepsilon_{r\theta}}{\partial r} - \frac{1}{r}\frac{\partial\varepsilon_{rr}}{\partial\theta} + \frac{2\varepsilon_{r\theta}}{r}\right)\right\} \tag{7a}$$

$$H_\theta = -\frac{1}{\varepsilon_{rr}^2 + \varepsilon_{r\theta}^2}\left\{\varepsilon_{r\theta}\left(\frac{\partial\varepsilon_{rr}}{\partial r} + \frac{1}{r}\frac{\partial\varepsilon_{r\theta}}{\partial\theta} + \frac{2\varepsilon_{rr}}{r}\right)\right.$$
$$\left. - \varepsilon_{rr}\left(\frac{\partial\varepsilon_{r\theta}}{\partial r} - \frac{1}{r}\frac{\partial\varepsilon_{rr}}{\partial\theta} + \frac{2\varepsilon_{r\theta}}{r}\right)\right\} \tag{7b}$$

where $\varepsilon_{\theta\theta}$ and $\varepsilon_{r\theta}$ are the tangential and shear components of the strain tensor, respectively.

As a mathematical criterion to extract the inclusion contours, knowing the intraplaque strain field, the norm of the vector $\vec{H}$ can be satisfactory used as a criterion function. However, we chose the following criterion function expression:

$$dW = \vec{H}.d\vec{x} \tag{8}$$

where $d\vec{x}$ is the elementary position vector. Interestingly, this equation provides direct relationship between dW and the relative variation of the local Young's modulus.

Indeed, by using (5), (6) and (8), dW may be interestingly expressed as

$$dW = \left(\frac{\nabla E}{E} - \frac{3}{2}[\varepsilon]^{-1}\frac{\nabla p}{E}\right).d\vec{x}$$
$$= \frac{dE}{E} - \frac{3}{2}[\varepsilon]^{-1}\frac{\nabla p}{E}.d\vec{x}. \tag{9}$$

Equation (9) shows that approximation of dW by dE/E will be all the more accurate since the components of the Lagrange multiplier gradient become small.
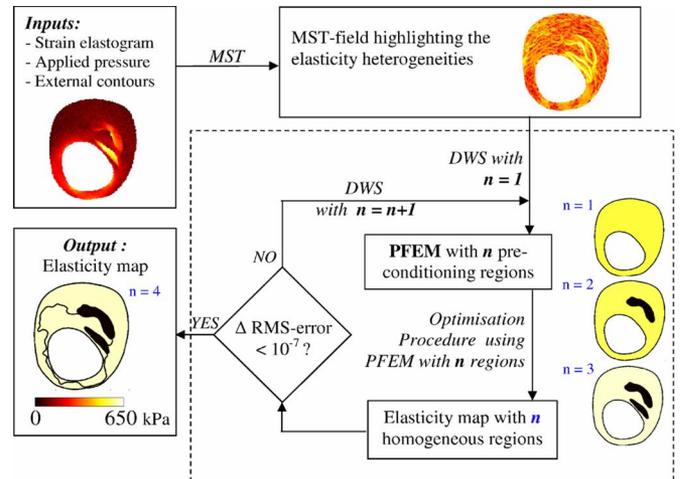

Fig. 2. Description of the successive steps performed in our reconstruction algorithm in order to highlight the spatial repartition of the Young modulus. A detailed description of each step is given in the text.

In practical situations, the radial strain is the most reliable estimate of the strain tensor with current elastography techniques [19], [47]. Therefore, we simplified our criterion by neglecting the shear strains. So, the expression of the criterion function dW is now given, when one considers the abovementioned hypotheses, by

$$dW = -\frac{1}{\varepsilon_{rr}}\left(\frac{\partial\varepsilon_{rr}}{\partial r} + \frac{2\varepsilon_{rr}}{r}\right)dr - \frac{1}{\varepsilon_{rr}}\frac{\partial\varepsilon_{rr}}{\partial\theta}d\theta. \tag{10}$$

The two partial derivatives of the radial strain component [(10)] were computed by convoluting the strain field image with 5×5 Sobel's masks (procedure imfilter, Image Processing Toolbox, MATLAB, release R14, The MathWorks). Then, the amplitude of dW was computed on the defined regular polar mesh described below to obtain the MST-image. The contours of each region correspond to the lines where the amplitude of the criterion function dW was the highest. This mathematical pre-conditioning procedure was called "Modified Sumi's Transform" (MST) and was used to highlight plaque heterogeneities.

2) Young's Modulus Reconstruction: Fig. 2 schematizes the successive steps of the proposed inverse approach to identify the elasticity map from the radial strain field using a parametric finite element model (PFEM). Based on the obtained MST-field, a dynamic watershed segmentation (DWS) (procedure watershed, Image Processing Toolbox, MATLAB, release R14, The MathWorks) combined with an optimization procedure was applied to obtain the modulogram of the studied plaque (Fig. 2). This combined procedure was named "DWS-O."

At each iteration of the watershed segmentation procedure (i.e., for a given number of plaque inclusions n), we assumed that each inclusion had a uniform stiffness. The n Young's moduli were then identified using a gradient-based optimization procedure (procedure fmincon, Optimization Toolbox, MATLAB, release R14, The MathWorks) which minimized the root mean squared error ($\text{rms}_{\text{plaque-error}}$) between the

measured $\varepsilon_{rr}^{\mathrm{meas}}$ and the computed $\varepsilon_{rr}^{\mathrm{comp}}$ radial strains inside the plaque

$$\mathrm{rms}_{\text{plaque-error}} = \sqrt{\frac{1}{N} \sum_{\text{node},i} [\varepsilon_{rr}^{\mathrm{meas}}(n_i) - \varepsilon_{rr}^{\mathrm{comp}}(n_i)]^2} \quad (11)$$

where N is the total number of nodes in the plaque mesh and n_i the plaque node i of the regular polar mesh.

One constraint was imposed during the optimization procedure: the unknown Young's moduli were ranged between 10^{-1} kPa and 10^4 kPa. In this process, a Young's moduli set solution was found acceptable when the gradient-based optimization procedure reached either a tolerance termination value lower than 10^{-8} or a maximum number of iterations equal to 30 [27].

More refined segmentations were obtained from the DWS procedure by increasing the number n of plaque inclusions up to a maximum value of $n = 10$. Indeed, we know from plaque morphology studies on vulnerable plaques [4] that this is a realistic upper boundary. Additionally, from a computational point of view, we will verify *a posteriori* (see Section III-D) that this upper limit is never reached during the optimization process. The increase of preconditioning sites took into account smaller changes in Young's modulus (i.e., smaller values of the dW-field). So, at the early stage of the DWS procedure, the most abrupt changes in Young's modulus were taken into account and then progressively minor changes were considered. Thus, when a Young's moduli set solution has been obtained for a given number of preconditioning regions, the next iteration of the watershed segmentation procedure was started. The DWS was initiated with one region (i.e., $n = 1$). The DWS procedure was stopped when the absolute $\mathrm{rms}_{\text{plaque-error}}$ variation between two successive iterations n and $n + 1$ (i.e., $\Delta\mathrm{rms}_{\text{plaque-error}}$) became lower than a threshold value of 10^{-7}.

III. RESULTS

A. IVUS Study

Five nonruptured plaques with necrotic cores and calcium inclusions were identified after the extensive IVUS scanning. Distinct and multiple ruptured plaques were observed in each patient, but nonruptured plaques were not systematically found. Table I summarizes the geometrical features of the five plaques scanned *in vivo* and the two idealized plaques mimicking the thinning of the cap occurring during the growth process.

B. Performance of the Algorithm

Excepted when it is mentioned, all results were derived from radial strain fields with default noise (i.e., with $\beta = 1$). For clarity reasons, simplified Young's modulus maps are often presented by grouping together preconditioning regions of close stiffness. Means and standard deviations of the Young's moduli of the grouped regions are given.

1) Validation of the Segmentation Procedure: To test the performance of the segmentation algorithm, we compared the computed contours of the plaque constituents to the real ones by using the following indexes: 1) the positive predictive value

TABLE I
DESCRIPTION OF PLAQUE CHARACTERISTICS DETECTED BY IVUS

Plaque #	Origin of the Geometry	Cap Thickness (µm)	Necrotic Core Areas (mm²)	Calcium Area (mm²)	Plaque Area (mm²)	Lumen Area (mm²)	Degree of Stenosis (%)
1	IVUS	369	1.604	-	19.735	8.403	70
2	Model	174	2.29	-	19.735	8.403	70
3	Model	103	2.37	-	19.735	8.403	70
4	IVUS	204	5.557	-	16.961	3.085	85
5	IVUS	147	0.505/ 1.196	-	17.822	6.736	73
6	IVUS	199	1.996	0.356	17.704	3.548	83
7	IVUS	214	2.151 / 0.701	0.891	16.730	3.575	82

(PPV), defined as the ratio between the "true positive area" and the union of the "true positive area" with the "false positive area" and 2) the sensitivity value (SV), defined as the ratio between the "true positive area" and the union of the "true positive area" with the "false negative area" (this last union is also the real area) [48]. Whatever the considered plaque (i.e., Plaque #1–7), the indexes PPV and SV were always greater than 81% and 89% for necrotic cores contours, and greater than 79% and 81% for calcium inclusions contours, respectively. Thus, these high indexes values indicate a good agreement between real and computed contours (data not shown).

2) Detection of Soft Inclusions: Fig. 3 shows elasticity maps obtained for vulnerable plaques with one (Plaque #4) and two necrotic cores (Plaque #5), respectively. The combined MST and DWS-O procedures were successfully used to estimate the Young's modulus distribution with an optimum number of iterations ($n = 3$ and 4, respectively). The quite complex shapes of the different necrotic cores were also accurately reconstructed. However, the error made on necrotic core Young's moduli appears to be larger for plaques with several neighboring soft cores (Fig. 3, Plaque #5) than for those with only one soft inclusion (Fig. 3, Plaque #4).

3) Quantification of $\mathrm{Cap}_{\text{thick}}$ *and* $\mathrm{Core}_{\text{area}}$: Fig. 4 illustrates the performance of our algorithm to detect three vulnerable lesions with values $\mathrm{Cap}_{\text{thick}}/\mathrm{Core}_{\text{area}}$ equal to 369 μm/1.604 mm², 174 μm/2.290 mm² and 103 μm/2.370 mm², respectively. Our results show that $\mathrm{Core}_{\text{area}}$ and $\mathrm{Cap}_{\text{thick}}$ were well estimated with maximum relative errors lower than 1% (Plaque #1) and 16% (Plaque #2), respectively.

4) Detection of Calcium Inclusions: For both plaque morphologies (Plaques #6 and 7) with necrotic cores and calcium inclusions presented in Fig. 5, the combined MST and DWS-O procedures reconstructed successfully the elasticity maps with an optimum number of unknown Young's moduli of 4 and 5, respectively. The proposed algorithm detected accurately all inclusion contours. However, the elasticity of the calcified medium appears to be underestimated by almost a factor two.

C. Influences of Artifact Measurements On Young's Modulus Reconstruction

1) Influence of White Noise: Figs. 6 and 7 highlight the robustness of the algorithm when increasing the white noise level. The influence of noise was studied on a vulnerable plaque with a $\mathrm{Cap}_{\text{thick}}$ equals to 103 μm (Plaque #3). According to these
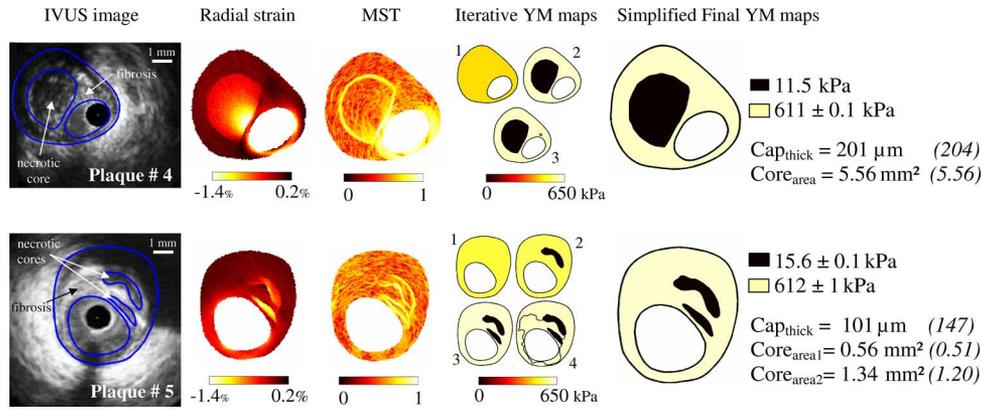
Fig. 3. Performance of the method to detect vulnerable plaques. Plaques #4 and 5 with one and two necrotic cores, respectively, were used for this investigation. Column 1: IVUS images and plaque morphologies. Column 2: Perturbed radial strain fields obtained with blood pressure of 1 kPa and a default white noise ($\beta = 1$). Column 3: Spatial derivative fields of the Young's modulus resulting from the modified Sumi's transform (MST) procedure. Column 4: Evolution of the Young's modulus (YM) map obtained during the execution of the combined dynamic Watershed Segmentation and optimization procedure (DWS-O). Column 5: Final Young's Modulus maps and resulting estimations of cap-thickness ($\mathrm{Cap_{thick}}$) and necrotic cores areas ($\mathrm{Core_{area}}$). In parenthesizes are given the target values, and the targeted fibrosis and the necrotic cores Young's moduli were 600 and 10 kPa, respectively.
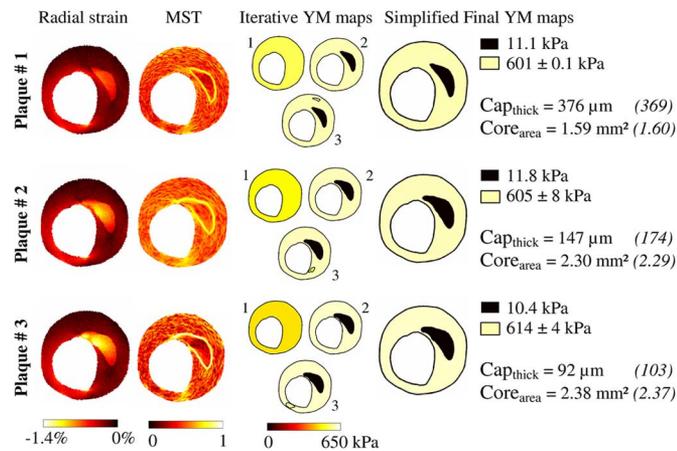

Fig. 4. Performance of the method to detect cap thickness. Plaques #1–3 were used for these simulations. Column 1: Perturbed radial strain fields obtained with blood pressure of 1 kPa and a default white noise. Column 2: Spatial derivative fields of the Young's modulus resulting from the modified Sumi's transform (MST) procedure. Column 3: Evolution of the Young's modulus (YM) map obtained during the execution of the combined dynamic watershed segmentation and optimization procedure (DWS-O). Column 4: Final Young's Modulus maps and resulting estimations of cap-thickness ($\mathrm{Cap_{thick}}$) and necrotic cores areas ($\mathrm{Core_{area}}$). In parenthesizes are given the target values, and the targeted fibrosis and the necrotic cores Young's moduli were 600 kPa and 10 kPa, respectively.

figures, the algorithm still gave reasonable results when introducing significant white noise amplitude ($\beta = 6$). The mean number of preconditioning regions found at the end of the identification procedure increased with noise amplitude: from 3.5 with a default white noise ($\beta = 1$) to 6.2 with a noise six times higher ($\beta = 6$) (Fig. 6). At high level of noise, the $\mathrm{Cap_{thick}}$ was underestimated by approximately 15% [Fig. 7(a)] while the $\mathrm{Core_{area}}$ varied slightly (lower than 5%) [Fig. 7(b)]. The core Young's modulus amplitude was more sensitive to noise than the Young's modulus of fibrosis [Fig. 7(c) and (d)].

2) Influence of Catheter Position on Young's Modulus Reconstruction: The influence of the catheter position was investigated on a vulnerable plaque morphology with one necrotic

core and a $\mathrm{Cap_{thick}}$ equals to 103 μm (Plaque #3). Very similar stiffness maps were found when considering distinct strain fields simulated with different catheter positions and with standard noise ($\beta = 1$) (Fig. 8). The $\mathrm{Core_{area}}$, the necrotic core and fibrosis Young's moduli were estimated with less than 2%, 17%, and 2% of error, respectively. Nevertheless, when the catheter was located near the necrotic core [Fig. 8(a)]. The $\mathrm{Cap_{thick}}$ was overestimated by 58%. The shape of the soft inclusion was also influenced by the catheter position but with a limited impact on the final Young's modulus reconstruction.

3) Influence of Surrounding Tissue: Simulations analyzing the influence of the surrounding tissue were performed on one vulnerable plaque geometry (Plaque #3). The surrounding tissue was modeled as an external layer with constant Young's modulus of 300 kPa and relative thickness ranging from 1.5 to 10. We found that the thickness of the surrounding tissue leads to an overestimation of the computed stiffness of the fibrosis (maximal relative error of 45%). Conversely, the stiffness of the necrotic core was underestimated (maximal relative error of -24%). These maximal relative errors were obtained as soon as the relative thickness of the external layer reaches a critical value equal approximately to 2.5. This ratio is indeed the value considered in our simulations investigating the effects of the external layer stiffness. The existence of such a threshold is commonly reported and interpreted as a limit of validity for semi-infinite medium approximation considered in elasticity problems involving two interacting solids [49].

Regarding the effect of the surrounding tissue stiffness, we found that whatever the Young's modulus considered (varying from 1 to 600 kPa), the algorithm identified reasonably the vulnerable plaque morphology ($\mathrm{Cap_{thick}} = 95 \pm 3\ \mu$m and $\mathrm{Core_{area}} = 2.293 \pm 0.015\ \mathrm{mm}^2$, for targets equal to 103 μm and 2.370 mm^2, respectively). The reconstructed Young's moduli of the fibrosis and of the necrotic core respectively increased and decreased with the stiffening of the surrounding medium (Fig. 9). Indeed, when the surrounding tissue stiffness was at the maximum of 600 kPa, the identified Young's modulus of the fibrosis was overestimated by 66%, while that of the necrotic
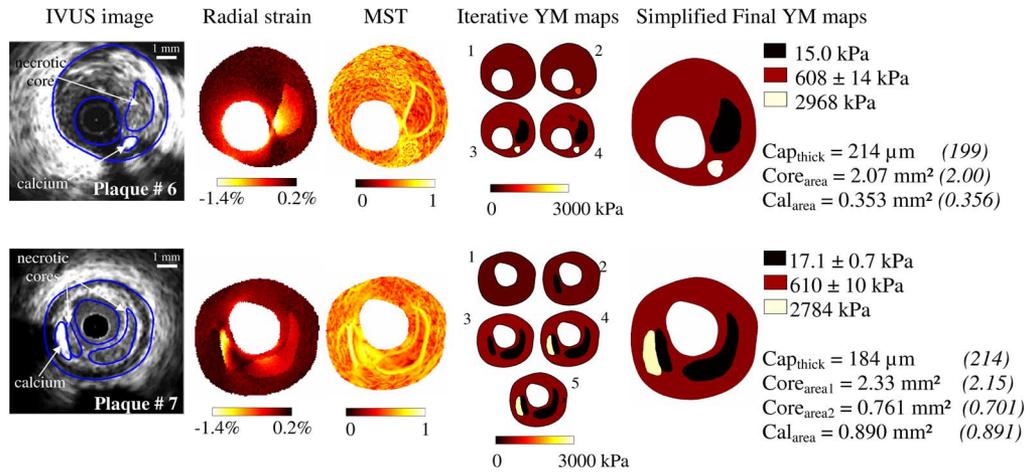
Fig. 5. Performance of the method to detect plaques with calcium inclusions. Plaques #6 and 7 with necrotic cores and calcium inclusions were used for this investigation. Column 1: IVUS images and plaque morphologies. Column 2: Perturbed radial strain fields obtained with blood pressure of 1 kPa and a default white noise. Column 3: Spatial derivative fields of the Young's modulus resulting from the modified Sumi's transform (MST) procedure. Column 4: Evolution of the Young's modulus (YM) map obtained during the execution of the combined dynamic Watershed Segmentation and optimization procedure (DWS-O). Column 5: Final Young's modulus maps and resulting estimations of cap-thickness (Cap_{thick}) and necrotic cores areas ($Core_{area}$). In parenthesizes are given the target values, and the targeted fibrosis, necrotic cores and calcium Young's moduli were 600 kPa, 10 kPa and 5000 kPa, respectively.
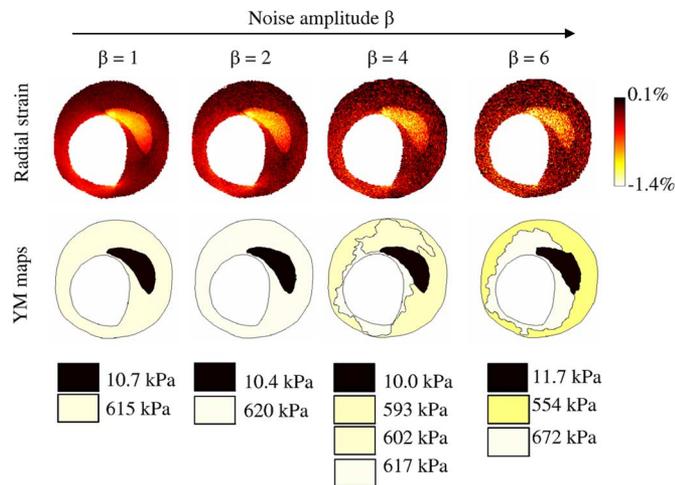

Fig. 6. Sensitivity analysis performed to investigate the influence of the white noise on Young's modulus (YM) maps. Plaque #3 was used for this study. Row 1: Input radial strain elastograms simulated with different level of white noise ranging from β equal 1 to 6. Row 2: Resulting Young's modulus maps obtained with our algorithm.

Fig. 7. Influence of white noise amplitude on estimations of cap thickness (Cap_{thick}), necrotic core area ($Core_{area}$) and Young's moduli of the necrotic core (E_{core}) and fibrosis ($E_{fibrosis}$). Plaque #3 was used for this investigation. Knowing that the noise was spatially randomly distributed, we performed 15 computations for each amplitude of noise β and present the mean values $\pm$ the standard deviations. The target values are the dashed lines. A: Influence of noise on Cap_{thick} value. B: Influence of noise on $Core_{area}$ value. C: Influence of noise on E_{core} value. D: Influence of noise on $E_{fibrosis}$ value.

core was underestimated by 33%. However, if the surrounding tissue stiffness was added as an unknown stiffness parameter to reconstruct, the algorithm successfully identified the Young's moduli of the fibrosis ($594 \, \text{kPa} \pm 16 \, \text{kPa}$, for a target equals to 600 kPa) and of the necrotic core ($10.1 \, \text{kPa} \pm 0.2 \, \text{kPa}$, for a target equals to 10 kPa). Thus, the surrounding tissue stiffness could also be identified with a maximum relative error of less than 8% (Fig. 9).

D. Comparison Between the MST and the SKT Preconditioning Procedures

The algorithm can use different image transforms during the preprocessing step. In this section we compare the performance of the DWS-O procedure when using MST or Skovoroda's
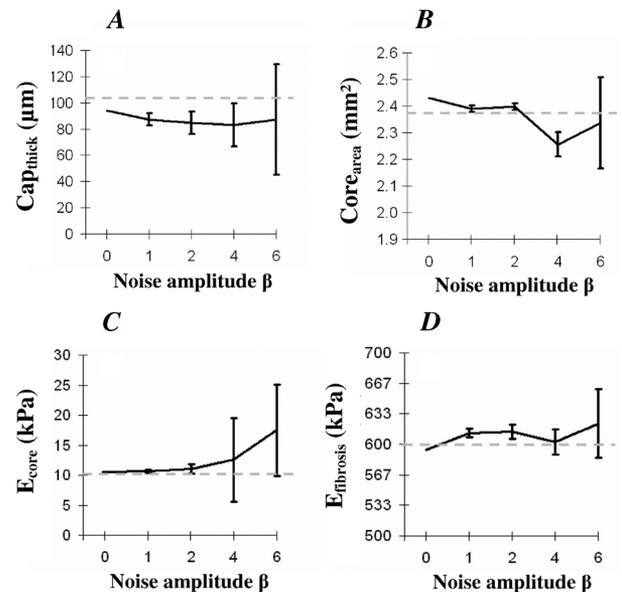
transform (SkT). Both image transforms were used to reconstruct the elasticity maps from a known strain field with standard noise ($\beta = 1$). This comparison was performed on two plaque morphologies (Plaques #3 and #7).

For simulations performed with Plaque #3 that had only one soft heterogeneity, results found with both methods were similar [Fig. 10(a)]. However, for more complex lesions with two necrotic cores and one calcified inclusion as Plaque #7, the MST approach appeared more accurate and efficient. Indeed,
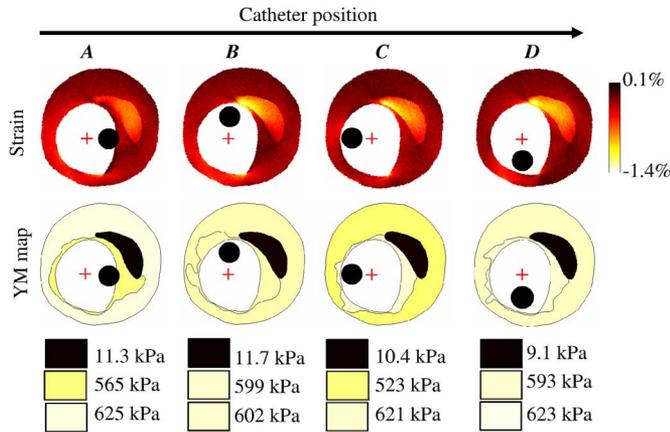
Fig. 8. Influence of the catheter position on the reconstruction of the Young's modulus (YM) maps. The simulated radial strain fields were computed for four different catheter positions. Plaque #3 was used for these simulations.
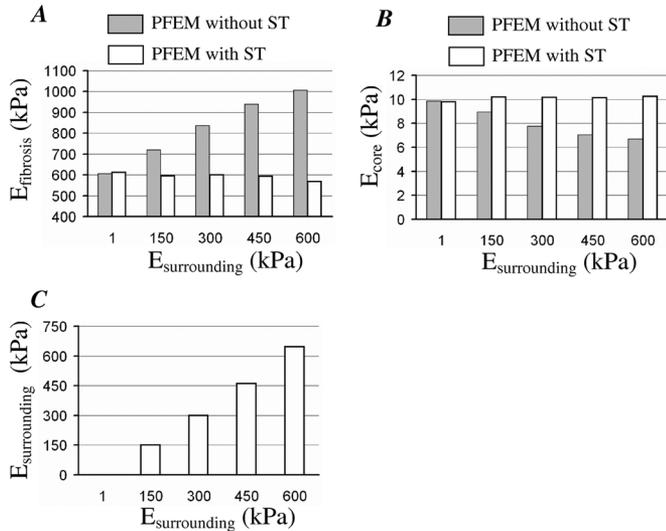

Fig. 9. Influence of the surrounding tissue rigidity on the identification of the necrotic core and fibrosis stiffness. Plaque #3 was used for these simulations. Identified fibrosis (A), necrotic core (B), and (C) surrounding tissue Young's moduli as a function of the surrounding tissue stiffness which was used to simulate the input strain elastogram.
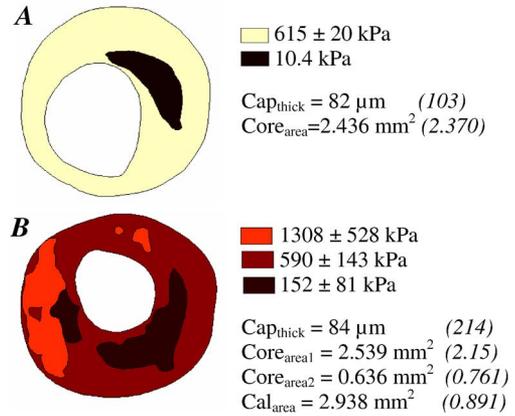

Fig. 10. Elasticity reconstructions based on the Skovoroda transform (SkT) procedure. A) Simulation performed with Plaque #3. B) Simulation performed with Plaque #7. Final Young's Modulus maps and resulting estimations of cap-thickness ($\mathrm{Cap_{thick}}$), necrotic cores areas ($\mathrm{Core_{area}}$) and calcium inclusion areas ($\mathrm{Cal_{area}}$). In parenthesizes are given the target values, and the targeted fibrosis, necrotic cores, and calcium Young's moduli were 600 kPa, 10 kPa, and 5000 kPa, respectively.
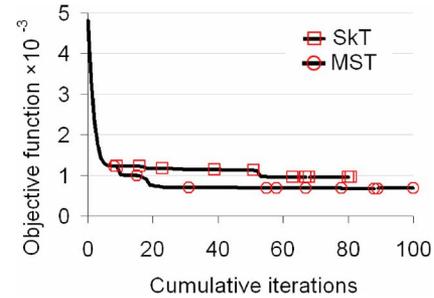

Fig. 11. Variation of the rms error as a function of the number n of preconditioning regions and cumulated iteration number of the gradient-based optimization procedure, during the reconstruction of the Young modulus map. Plaque # 7 was used for these simulations. MST: Modified Sumi's transform. SkT: Skovoroda's transform.

by using the SkT preconditioning procedure, the necrotic core Young's modulus was dramatically overestimated by a factor of 14, the calcium stiffness was largely underestimated by 74% while the $\mathrm{Cap_{thick}}$ was underestimated by 61% [Fig. 10(b)]. Reconstructing the Young's modulus distribution using the MST was more successful (Fig. 5, Plaque #7). Indeed, the errors made on the elasticity map and geometrical plaque feature estimations remained reasonable. However, for both methods, the relative errors made on the Young's modulus of the calcified inclusion were still important.

Fig. 11 shows the evolution of the $\mathrm{rms_{plaque\text{-}error}}$ as a function of the number of preconditioning regions within the DWS-O procedure for the simulation performed with Plaque #7. We forced the algorithm to run up to $n = 10$ preconditioning regions. When using the MST procedure, the $\mathrm{rms_{plaque\text{-}error}}$ decreased rapidly and reached a stable minimum value after only $n = 5$ iterations. At this stage, all components and

contours were accurately identified. On the contrary, when using the SkT procedure, the $\mathrm{rms_{plaque\text{-}error}}$ decreased at a lower rate, and after $n = 8$ iterations, it became acceptable but mechanical properties and boundaries of the plaque heterogeneities were not well defined. Note that, even after $n = 10$ iterations, the SkT procedure was found not efficient enough for the characterization of such complex plaques (Fig. 11).

IV. DISCUSSION

Characterizing the mechanical properties of vulnerable plaque components is a major issue, as it could lead to the development of specific treatment strategies for the prevention of acute thrombotic events [50]. In spite of the fact that mechanical strain fields can be approximated and measured *in vivo* quite reasonably, thanks to endovascular elastography methods [19]–[22], determination of plaque elastic Young's moduli, plaque inclusions and cap thickness remain difficult to assess for complex plaque morphologies.

A priori information was shown to be imperatively needed to constrain the resolution of the inverse problem when using iterative approaches so that a unique reconstructed rigidity map could be found from the strain/displacement fields [28], [51],

[52]. To constrain the optimization algorithm, Chandran *et al.* [30] identified equi-rigidity regions before their iterative procedure. Other groups [29], [35], [38] used medical images to directly derive the plaque morphology so that the geometry of the components was already known before the reconstruction process. Aglyamov [26] used concentric circles representing the different layers of a vein subjected to thrombosis, whereas Baldewsing [27] used nonconcentric circles to model the plaque inclusions. An elegant method using adaptive Bezier curves [41] was considered to take into account more complex necrotic core geometries. In this last work, the curves were iteratively modified by using a PFEM. Following the spirit of this group, we designed a PFEM which originally reinitializes automatically and dynamically the inverse problem by progressively detecting all plaque constituents. With regard to other techniques, two major advantages can be stated.

1) We do not need to add any geometrical parameters (like Bezier curves) into our PFEM to adjust the shapes of the plaque inclusions during the optimization procedure as the initial plaque geometry obtained with the combined MST/DWS-O procedure is close to the real plaque morphology.

2) The case of heterogeneous plaques with several soft and/or hard inclusions can be reconstructed by a unique procedure which takes into account the mechanical interactions between the different plaque heterogeneities.

In the current study, the original PFEM was successfully tested and validated on several plaque morphologies acquired from patients who underwent coronary IVUS. Interestingly, this preliminary work which presents the theoretical framework of our approach has shown that the developed coupled MST/DWS-O procedure is efficient and robust for the detection of sites of heterogeneity as well as for the estimation of the cap thickness and modulogram even for complex plaque morphologies constituted of several soft and hard inclusions.

A. Successful Characterization of Complex Plaque Morphologies

1) Lesions With Single and Multiple Necrotic Cores: For simple vulnerable plaques with one necrotic core, the MST together with the DWS-O procedures were able to spatially constrain the inverse problem using a small number of regions of uniform Young's moduli. Indeed, the MST gave enough information to the DWS-O to segment the necrotic core at the first iteration, leading to a fast reconstruction of the rigidity map. Let us notice that by comparison, for similar plaques with a thin cap and one necrotic core, a previous study used five additional geometric parameters to adjust the shape of the soft inclusion [41]. As the geometry of the necrotic core was directly identified by the MST combined with the DWS-O, the optimization of its shape was not necessary. Our algorithm also appeared to be efficient in cases of plaques with several necrotic cores and the mechanical interaction between all cores was taken into account, which constitutes another original feature of our method.

2) Is This Algorithm Adapted to Detect Vulnerable Plaques?: Devoted to further clinical studies, the algorithm seems able to detect quite reasonably small $\text{Cap}_{\text{thick}}$ amplitudes and $\text{Core}_{\text{area}}$ during simulations of plaque growth. These parameters are

known to be the major clinical criteria for predicting plaque vulnerability [3]. For the atheroma lesion with the highest degree of vulnerability considered in this study (Plaque #3 which had a $\text{Cap}_{\text{thick}}$ of 103 μm), the algorithm was still able to detect accurately the $\text{Cap}_{\text{thick}}$ even with an important level of noise (Fig. 6). Note that this performance was directly linked with the radial resolution of 36 μm used in our polar mesh grid, which was adapted to the resolution of the Lagrangian Speckle Model Estimator method developed by Maurice *et al.* [21]. Thus, the lower $\text{Cap}_{\text{thick}}$ that can be detected with such a method is in the order of the radial resolution of the input strain elastogram.

3) Is This Algorithm Adapted to Detect Calcium Inclusions?: Several groups outlined that calcium inclusions in the fibrous cap could play an important role in the mechanical stress/strain distributions and in some instance could increase the vulnerability of the plaque [5], [53]–[57]. Therefore, we investigated the performance of our algorithm to also detect calcified inclusions within heterogeneous plaques. The proposed algorithm successfully identified all calcium inclusions. However, because of noise that stands in regions of small strain amplitudes, the estimated Young's moduli were largely underestimated but remained high enough as to reveal presence of rigid heterogeneities (Fig. 5).

4) Do We Need to Model the Surrounding Tissue?: In most vascular modulography methods, the surrounding tissue is omitted. It was shown for homogeneous monolayer cases [20] that the stiffness of the surrounding tissue affects the strain distribution within the arterial wall. We confirmed this study by showing that the identified stiffness of the fibrosis was overestimated by almost 66% when the surrounding tissue stiffness was close to the stiffness of the fibrosis itself. So we must be aware that potential hard surrounding tissue may bias the plaque stiffness by increasing it up to a factor of two if the surrounding tissue is not considered. Interestingly, the stiffness of the soft core seemed to be not significantly affected by such additional medium. Thus, the parametric finite element model (PFEM) would be more performing for clinical applications if we consider also the Young's modulus of the surrounding tissue as an additional unknown. However, this would impose the knowledge of the external layer thickness, which appears to be a real challenge today with the IVUS technique.

5) Performance of the Algorithm When Using Also the Shear Strain as Input Elastograms: Interestingly, Maurice *et al.* [21] showed that the shear strain field could be evaluated using intravascular elastography (IVE). Therefore, the performance of the proposed algorithm is discussed for Plaque #3 when using both the radial strain and the shear strain as the input elastograms. The MST criterion dW was calculated using (7a) and (7b), and the RMS error was computed using the shear strain and the radial strain fields. Reconstructed $\text{Cap}_{\text{thick}}$, $\text{Core}_{\text{area}}$, Young's moduli of the necrotic core and fibrosis were found equal to: 87 μm (relative error of -16%), 2.321 mm^2 (relative error of -2%), 10.1 kPa (relative error of $+1\%$) and 603 ± 15 kPa (relative error of less than $+1\%$), respectively. Thus, in this case, the reconstruction of the stiffness map and plaque morphology appeared slightly improved (lower than 2%) when considering also the shear strain elastogram.

B. Study Limitations

Several limitations deserve to be pointed out at this stage, even if the present study does highlight original and potentially promising concepts for improving vulnerable plaque identification from strain measurements.

1) In order to take into account the 2-D aspect of the IVUS image acquisition, our structural analysis was performed in two dimensions, assuming plane strain condition. Such an assumption is, however, reasonable insofar as plaque length is large with regard to the radial dimension [58].

2) A gradient based descent algorithm was used in the optimization process. However, more efficient algorithms could be selected [35], [59]–[62], which would give better results in term of calculation time.

3) In all the FE simulations, static loading conditions were also applied. These conditions did not consider the pulsatile nature of physiological blood pressure. Thus, the time-dependent viscoelastic effects due to the cyclic loading imposed by blood flow in the arteries [63], [64] were not taken into account, nor were the anisotropic nonlinear elastic components of the plaque's mechanical behavior [65], [66]. However, it is legitimate to neglect such nonlinear effects when a small blood pressure differential is used. Assuming isotropic constituents allows us to reconstruct only the homogenized Young's modulus map, which interestingly appears to be sufficient to highlight vulnerable plaques.

4) The influence of residual strains [66]–[68], generated by remodeling and plaque growth processes, have been ignored in this study. Taking them into account would probably bias the plaque morphology by introducing virtual regions in the plaque that would be interpreted abusively as additional soft or rigid heterogeneities.

5) Only simulated input strain elastograms based on real plaque morphologies were used in this study. This should, however, be seen in the light of our aim, which was as a first step to present the theoretical framework and test the performances of the proposed vascular elastography algorithm.

C. Relevance for Other Clinical Applications

Several additional processes are known to be involved in the plaque rupture mechanism, including plaque erosion [1], tissue degradation due to macrophages [1], [3], and biological activities responsible for the cellular inflammatory reaction [1], [69]–[73]. Indeed, many studies of structural variations of the fibrous cap and necrotic core were reported, namely those focusing on inflammatory processes aggravating plaque vulnerability and those on statin treatment enhancing plaque stability [50]. It has been shown that the peak cap-stress amplitude—a predictor of plaque rupture—varies exponentially not only with $\mathrm{Cap_{thick}}$ but also with the Young's modulus of the necrotic core [16]. This shows how very slight structural changes can tilt a vulnerable plaque from stability to instability or vice versa. Such small changes may either "precipitate" rupture or, conversely, "stabilize" a vulnerable plaque. Swings of this sort could only be observed in clinical setting with such modulography methods.

REFERENCES

[1] V. Fuster, P. R. Moreno, Z. A. Fayad, R. Corti, and J. J. Badimon, "Atherothrombosis and high-risk plaque: Part I: Evolving concepts," *J. Am. College. Cardiol.*, vol. 46, pp. 937–54, 2005.

[2] W. Koenig, "Inflammation and coronary heart disease: An overview," *Cardiol. Rev.*, vol. 9, pp. 31–5, 2001.

[3] M. Naghavi *et al.*, "From vulnerable plaque to vulnerable patient: A call for new definitions and risk assessment strategies: Part I," *Circulation*, vol. 108, pp. 1664–72, 2003.

[4] R. Virmani, A. P. Burke, A. Farb, and F. D. Kolodgie, "Pathology of the vulnerable plaque," *J. Am. College. Cardiol.*, vol. 47, pp. C13–8, 2006.

[5] S. G. Carlier and K. Tanaka, "Studying coronary plaque regression with IVUS: A critical review of recent studies," *J. Interv. Cardiol.*, vol. 19, pp. 11–5, 2006.

[6] G. Rioufol *et al.*, "Multiple atherosclerotic plaque rupture in acute coronary syndrome: A three-vessel intravascular ultrasound study," *Circulation*, vol. 106, pp. 804–8, 2002.

[7] I. K. Jang *et al.*, "Visualization of coronary atherosclerotic plaques in patients using optical coherence tomography: Comparison with intravascular ultrasound," *J. Am. College Cardiol.*, vol. 39, pp. 604–9, 2002.

[8] T. Kubo *et al.*, "Assessment of culprit lesion morphology in acute myocardial infarction: Ability of optical coherence tomography compared with intravascular ultrasound and coronary angioscopy," *J. Am. College Cardiol.*, vol. 50, pp. 933–9, 2007.

[9] Z. A. Fayad, V. Fuster, K. Nikolaou, and C. Becker, "Computed tomography and magnetic resonance imaging for noninvasive coronary angiography and plaque imaging: Current and potential future concepts," *Circulation*, vol. 106, pp. 2026–34, 2002.

[10] K. C. Briley-Saebo *et al.*, "Magnetic resonance imaging of vulnerable atherosclerotic plaques: Current imaging strategies and molecular imaging probes," *J. Magn. Reson. Imag.*, vol. 26, pp. 460–79, 2007.

[11] H. M. Loree, R. D. Kamm, R. G. Stringfellow, and R. T. Lee, "Effects of fibrous cap thickness on peak circumferential stress in model atherosclerotic vessels," *Circ. Res.*, vol. 71, pp. 850–8, 1992.

[12] P. K. Shah, "Plaque size, vessel size and plaque vulnerability: Bigger may not be better," *J. Am. College Cardiol.*, vol. 32, pp. 663–4, 1998.

[13] R. Virmani, F. D. Kolodgie, A. P. Burke, A. Farb, and S. M. Schwartz, "Lessons from sudden coronary death: A comprehensive morphological classification scheme for atherosclerotic lesions," *Arterioscler Thromb Vasc. Biol.*, vol. 20, pp. 1262–75, 2000.

[14] A. Farb *et al.*, "Coronary plaque erosion without rupture into a lipid core. A frequent cause of coronary thrombosis in sudden coronary death," *Circulation*, vol. 93, pp. 1354–63, 1996.

[15] G. C. Cheng, H. M. Loree, R. D. Kamm, M. C. Fishbein, and R. T. Lee, "Distribution of circumferential stress in ruptured and stable atherosclerotic lesions. A structural analysis with histopathological correlation," *Circulation*, vol. 87, pp. 1179–87, 1993.

[16] G. Finet, J. Ohayon, and G. Rioufol, "Biomechanical interaction between cap thickness, lipid core composition and blood pressure in vulnerable coronary plaque: Impact on stability or instability," *Coronary Artery Disease*, vol. 15, pp. 13–20, 2004.

[17] D. D. Lee, K. Rigonan, and V. Dequattro, "Increased blood pressure and neural tone in the silent ischemia of hypertension: Disparate effects of immediate release nifedipine," *J. Am. College Cardiol.*, vol. 22, pp. 1438–45, 1993.

[18] J. Ohayon, P. Teppaz, G. Finet, and G. Rioufol, "In-vivo prediction of human coronary plaque rupture location using intravascular ultrasound and the finite element method," *Coronary Artery Disease*, vol. 12, pp. 655–63, 2001.

[19] C. L. de Korte *et al.*, "Morphological and mechanical information of coronary arteries obtained with intravascular elastography; feasibility study in vivo," *Eur .Heart J.*, vol. 23, pp. 405–13, 2002.

[20] K. Kim *et al.*, "Vascular intramural strain imaging using arterial pressure equalization," *Ultrasound Med. Biol.*, vol. 30, pp. 761–71, 2004.

[21] R. L. Maurice *et al.*, "On the potential of the lagrangian estimator for endovascular ultrasound elastography: In vivo human coronary artery study," *Ultrasound Med. Biol.*, vol. 33, pp. 1199–205, 2007.

[22] M. Wan, Y. Li, J. Li, Y. Cui, and X. Zhou, "Strain imaging and elasticity reconstruction of arteries based on intravascular ultrasound video images," *IEEE Trans. Biomed. Eng.*, vol. 48, no. 1, pp. 116–20, Jan. 2001.

[23] R. C. Chan, "OCT-based arterial elastography: Robust estimation exploiting tissue biomechanics," *Optics Express*, vol. 12, pp. 4558–4572, 2004.

[24] J. Rogowska, N. A. Patel, J. G. Fujimoto, and M. E. Brezinski, "Optical coherence tomographic elastography technique for measuring deformation and strain of atherosclerotic tissues," *Heart*, vol. 90, pp. 556–62, 2004.

[25] G. van Soest, F. Mastik, N. de Jong, and A. F. van der Steen, "Robust intravascular optical coherence elastography by line correlations," *Phys. Med. Biol.*, vol. 52, pp. 2445–58, 2007.

[26] S. Aglyamov, A. R. Skovoroda, J. M. Rubin, M. O'Donnell, and S. Y. Emelianov, "Model-based reconstructive elasticity imaging of deep venous thrombosis," *IEEE Trans. Ultrason. Ferroelectr. Freq. Control*, vol. 51, no. 5, pp. 521–31, May 2004.

[27] R. A. Baldewsing, J. A. Schaar, F. Mastik, C. W. Oomens, and A. F. van der Steen, "Assessment of vulnerable plaque composition by matching the deformation of a parametric plaque model to measured plaque deformation," *IEEE Trans. Med. Imag.*, vol. 24, no. 4, pp. 514–28, Apr. 2005.

[28] R. A. Baldewsing, J. A. Schaar, F. Mastik, and A. F. van der Steen, "Local elasticity imaging of vulnerable atherosclerotic coronary plaques," *Adv. Cardiol.*, vol. 44, pp. 35–61, 2007.

[29] D. Beattie, C. Xu, R. Vito, S. Glagov, and M. C. Whang, "Mechanical analysis of heterogeneous, atherosclerotic human aorta," *J. Biomech. Eng.*, vol. 120, pp. 602–7, 1998.

[30] K. B. Chandran *et al.*, "A method for in-vivo analysis for regional arterial wall material property alterations with atherosclerosis: Preliminary results," *Med. Eng. Phys.*, vol. 25, pp. 289–98, 2003.

[31] J. Fehrenbach, M. Masmoudi, R. Souchon, and P. Trompette, "Detection of small inclusions by elastography," *Inverse Problems*, pp. 1055–1055, 2006.

[32] N. H. Gokhale, "Nonlinear elasticity imaging using the adjoint method," Ph.D. dissertation, Boston Univ., Boston, MA, 2007.

[33] A. J. Hamilton *et al.*, "Regional material property alterations in porcine femoral arteries with atheroma development," *J. Biomech.*, vol. 38, pp. 2354–64, 2005.

[34] H. Kanai, H. Hasegawa, M. Ichiki, F. Tezuka, and Y. Koiwa, "Elasticity imaging of atheroma with transcutaneous ultrasound: Preliminary study," *Circulation*, vol. 107, pp. 3018–21, 2003.

[35] A. S. Khalil, B. E. Bouma, and M. R. K. Mofrad, "A combined FEM/genetic algorithm for vascular soft tissue elasticity estimation," *Cardiovasc. Eng.*, vol. 6, pp. 93–102, 2006.

[36] J. Luo, K. Ying, and J. Bai, "Elasticity reconstruction for ultrasound elastography using a radial compression: An inverse approach," in *Ultrasonics*, 2006, vol. 44, pp. e195–e198.

[37] F. A. Lupotti, "Vascular elasticity from regional displacement estimates," in *Proc IEEE Ultrason. Symp.*, 2003, vol. 2, pp. 1895–1898.

[38] L. Soualmi, M. Bertrand, R. Mongrain, and J. C. Tardif, "Forward and inverse problems in endovascular elastography," in *Acoustical Imaging*. New York: Plenum, 1997, pp. 203–209.

[39] D. A. Vorp, K. R. Rajagopal, P. J. Smolinski, and H. S. Borovetz, "Identification of elastic properties of homogeneous, orthotropic vascular segments in distension," *J. Biomech.*, vol. 28, pp. 501–12, 1995.

[40] A. H. Chau *et al.*, "Mechanical analysis of atherosclerotic plaques based on optical coherence tomography," *Ann. Biomed. Eng.*, vol. 32, pp. 1494–1494, 2004.

[41] R. A. Baldewsing, F. Mastik, J. A. Schaar, P. W. Serruys, and A. F. van der Steen, "Young's modulus reconstruction of vulnerable atherosclerotic plaque components using deformable curves," *Ultrasound Med. Biol.*, vol. 32, pp. 201–10, 2006.

[42] C. D. Mario *et al.*, "Clinical application and image interpretation in intracoronary ultrasound. Study group on intracoronary imaging of the working group of coronary circulation and of the subgroup on intravascular ultrasound of the working group of echocardiography of the european society of cardiology," *Eur . Heart J.* , vol. 19, pp. 207–29, 1998.

[43] R. A. Baldewsing, F. Mastik, J. A. Schaar, P. W. Serruys, and A. F. van der Steen, "Robustness of reconstructing the Young's modulus distribution of vulnerable atherosclerotic plaques using a parametric plaque model," *Ultrasound Med. Biol.*, vol. 31, pp. 1631–45, 2005.

[44] A. R. Skovoroda, S. Y. Emelianov, and M. O'Donnell, "Tissue elasticity reconstruction based on ultrasonic displacement and strain images," *IEEE Trans Ultrason. Ferroelectr. Freq .Control*, vol. 42, pp. 747–747, 1995.

[45] C. Sumi and K. Nakayama, "A robust numerical solution to reconstruct a globally relative shear modulus distribution from strain measurements," *IEEE Trans. Med. Imag.*, vol. 17, no. 3, pp. 419–28, Jun. 1998.

[46] A. E. Green and W. Zerna, *Theoretical Elasticity*. Oxford, U.K.: Clarendon, 1968.

[47] R. L. Maurice, J. Ohayon, G. Finet, and G. Cloutier, "Adapting the Lagrangian speckle model estimator for endovascular elastography: Theory and validation with simulated radio-frequency data," *J. Acoust. Soc. Am.*, vol. 116, pp. 1276–86, 2004.

[48] I. Levner and H. Zhang, "Classification-driven watershed segmentation," *IEEE Trans. Image Process.*, vol. 16, no. 5, pp. 1437–1445, May 2007.

[49] P. Tracqui and J. Ohayon, "Rotational microrheology of multilayered finite elastic media," *J. Appl. Phys*, vol. 102, pp. 1–6, 2007.

[50] P. Libby, "Current concepts of the pathogenesis of the acute coronary syndromes," *Circulation*, vol. 104, pp. 365–72, 2001.

[51] P. E. Barbone and J. C. Bamber, "Quantitative elasticity imaging: What can and cannot be inferred from strain images," *Phys. Med. Biol.*, vol. 47, pp. 2147–64, 2002.

[52] P. E. Barbone and N. H. Gokhale, "Elastic modulus imaging: On the uniqueness and nonuniqueness of the elastography inverse problem in two dimensions," *Inverse Problems*, pp. 283–283, 2004.

[53] K. Imoto *et al.*, "Longitudinal structural determinants of atherosclerotic plaque vulnerability: A computational analysis of stress distribution using vessel models and three-dimensional intravascular ultrasound imaging," *J. Am. College Cardiol.*, vol. 46, pp. 1507–15, 2005.

[54] C. Schmitt, G. Soulez, R. L. Maurice, M. F. Giroux, and G. Cloutier, "Noninvasive vascular elastography: Toward a complementary characterization tool of atherosclerosis in carotid arteries," *Ultrasound Med. Biol.*, vol. 33, pp. 1841–58, 2007.

[55] C. M. Shanahan, "Inflammation ushers in calcification: A cycle of damage and protection," *Circulation*, vol. 116, pp. 2782–5, 2007.

[56] D. Tang *et al.*, "Quantifying effects of plaque structure and material properties on stress distributions in human atherosclerotic plaques using 3D FSI models," *J. Biomech. Eng.*, vol. 127, pp. 1185–94, 2005.

[57] Y. Vengrenyuk *et al.*, "A hypothesis for vulnerable plaque rupture due to stress-induced debonding around cellular microcalcifications in thin fibrous caps," *Proc. Nat.Acad. Sci. USA*, vol. 103, pp. 14678–83, 2006.

[58] J. Ohayon, G. Finet, F. Treyve, G. Rioufol, and O. dubreuil, "A three-dimensional finite element analysis of stress distribution in a coronary atherosclerotic plaque: In-vivo prediction of plaque rupture location," *Biomechanics applied to computer assisted surgery*, pp. 225–241, 2005.

[59] M. Grédiac, E. Toussaint, and F. Pierron, "Special virtual fields for the direct determination of material parameters with the virtual fields method. 1—Principle and definition," *Int. J. Solids Struct.*, vol. 39, pp. 2691–2691, 2002.

[60] A. A. Oberai, N. H. Gokhale, M. M. Doyley, and J. C. Bamber, "Evaluation of the adjoint equation based algorithm for elasticity imaging," *Phys. Med. Biol.*, vol. 49, pp. 2955–74, 2004.

[61] J. J. Ou, R. E. Ong, T. E. Yankeelov, and M. I. Miga, "Evaluation of 3D modality-independent elastography for breast imaging: A simulation study," *Phys. Med. Biol.*, vol. 53, pp. 147–63, 2008.

[62] Z. Yong, L. O. Hall, D. B. Goldgof, and S. A. Sarkar, "A constrained genetic approach for computing material property of elastic objects," *IEEE Trans. Evolut. Computat.*, vol. 10, no. 3, pp. 341–341, Jun. 2006.

[63] C. Cheng *et al.*, "Atherosclerotic lesion size and vulnerability are determined by patterns of fluid shear stress," *Circulation*, vol. 113, pp. 2744–53, 2006.

[64] V. Gambillara, G. Montorzi, C. Haziza-Pigeon, N. Stergiopulos, and P. Silacci, "Arterial wall response to ex vivo exposure to oscillatory shear stress," *J. Vasc. Res.*, vol. 42, pp. 535–44, 2005.

[65] G. A. Holzapfel, G. Sommer, C. T. Gasser, and P. Regitnig, "Determination of layer-specific mechanical properties of human coronary arteries with nonatherosclerotic intimal thickening and related constitutive modeling," *Am. J. Physiol. Heart Circ. Physiol*, vol. 289, pp. H2048–58, 2005.

[66] D. Rehal, X. Guo, X. Lu, and G. S. Kassab, "Duration of no-load state affects opening angle of porcine coronary arteries," *Am. J. Physiol. Heart Circ. Physiol.*, vol. 290, pp. H1871–8, 2006.

[67] T. Matsumoto, T. Goto, T. Furukawa, and M. Sato, "Residual stress and strain in the lamellar unit of the porcine aorta: Experiment and analysis," *J. Biomech.*, vol. 37, pp. 807–15, 2004.

[68] J. Ohayon *et al.*, "Influence of residual stress/strain on the biomechanical stability of vulnerable coronary plaques: Potential impact for evaluating the risk of plaque rupture," *Am. J. Physiol. Heart Circ. Physiol.*, vol. 293, pp. H1987–96, 2007.

[69] L. H. Arroyo and R. T. Lee, "Mechanisms of plaque rupture: Mechanical and biologic interactions," *Cardiovasc. Res.*, vol. 41, pp. 369–75, 1999.

[70] A. C. Newby, "Do metalloproteinases destabilize vulnerable atherosclerotic plaques," *Curr Opin Lipidol*, vol. 17, pp. 556–61, 2006.

[71] K. Satoh *et al.*, "Important role of endogenous erythropoietin system in recruitment of endothelial progenitor cells in hypoxia-induced pulmonary hypertension in mice," *Circulation*, vol. 113, pp. 1442–50, 2006.

[72] J. C. Tardif *et al.*, "Effects of reconstituted high-density lipoprotein infusions on coronary atherosclerosis: A randomized controlled trial," *J. Am. Med. Assoc.*, vol. 297, pp. 1675–82, 2007.

[73] A. Tedgui and Z. Mallat, "Cytokines in atherosclerosis: Pathogenic and regulatory pathways," *Physiol. Rev.*, vol. 86, pp. 515–81, 2006.